Dalton Transactions

ROYAL SOCIETY OF CHEMISTRY

PAPER

View Article Online
View Journal | View Issue

Open Access Article. Published on 02 April 2024. Downloaded on 1/23/2026 10:42:30 PM.
This article is licensed under a Creative Commons Attribution-NonCommercial 3.0 Unported Licence.

Check for updates

Cite this: *Dalton Trans.*, 2024, **53**, 7527

A density functional theory analysis of the C–H activation reactivity of iron(IV)-oxo complexes with an 'O' substituted tetramethylcyclam macrocycle†

Lovleen Kaur and Debasish Mandal *

In this article, we present a meticulous computational study to foresee the effect of an oxygen-rich macrocycle on the reactivity for C–H activation. For this study, a widely studied nonheme Fe(IV)O molecule with a TMC (1,4,8,11-tetramethyl 1,4,8,11-tetraazacyclotetradecane) macrocycle that is equatorially attached to four nitrogen atoms (designated as N_4) and acetonitrile as an axial ligand has been taken into account. For the goal of hetero-substitution, step-by-step replacement of the N_4 framework with O atoms, *i.e.*, N_4, N_3O_1, N_2O_2, N_1O_3, and O_4 systems, has been considered, and dihydroanthracene (DHA) has been used as the substrate. In order to neutralise the system and prevent the self-interaction error in DFT, triflate counterions have also been included in the calculations. The study of the energetics of these C–H bond activation reactions and the potential energy surfaces mapped therefore reveal that the initial hydrogen abstraction, which is the rate-determining step, follows the two-state reactivity (TSR) pattern, which means that the originally excited quintet state falls lower in the transition state and the product. The reaction follows the hydrogen atom transfer (HAT) mechanism, as indicated by the spin density studies. The results revealed a fascinating reactivity order, in which the reactivity increases with the enrichment of the oxygen atom in the equatorial position, namely the order follows $N_4 < N_3O_1 < N_2O_2 < N_1O_3 < O_4$. The impacts of oxygen substitution on quantum mechanical tunneling and the H/D kinetic isotope effect have also been investigated. When analysing the causes of this reactivity pattern, a number of variables have been identified, including the reactant-like transition structure, spin density distribution, distortion energy, and energies of the electron acceptor orbital, *i.e.*, the energy of the LUMO ($\sigma^*_{z^2}$), which validate the obtained outcome. Our results also show very good agreement with earlier combined experimental and theoretical studies considering TMC and TMCO-type complexes. The DFT predictions reported here will undoubtedly encourage experimental research in this biomimetic field, as they provide an alternative with higher reactivity in which heteroatoms can be substituted for the traditional nitrogen atom.

Received 9th January 2024,
Accepted 29th March 2024

DOI: 10.1039/d4dt00063c

rsc.li/dalton

Introduction

Metal-oxo species of transition metal series are vastly studied, with the earlier members studied more prominently than the later ones owing to the oxo wall and the high-valence Fe(IV)O intermediates being studied in depth widely.[1–12] These complexes have been successfully presented in many articles wherein they act as active oxidants in the catalytic cycles of mononuclear non-heme and heme enzymes.[13–15] Multiple studies have also been conducted towards understanding the structural and electronic parameters of these metal-oxo complexes to get an idea how they drive towards better reactivity by accessing the mechanisms involved. For example, several octahedral/trigonal bipyramidal geometries have been explored wherein both $S = 1$ (triplet) and $S = 2$ (quintet) ground spin states have been taken into account.[16,17] It has been proven that spin states of Fe(IV) ions are an important governing factor affecting the catalytic activity of Fe(IV)O complexes. Studies in the last decade revealed that many changes have been projected in the coordination sphere directly in the form of axial as well as equatorial ligands, while other changes on the secondary level caused by manipulation of the ligand architecture have also been proven to have a significant effect on the mechanistic pathways.[18,19] Other factors such as the oxidative capabilities of different redox states have also gained attention

Department of Chemistry and Biochemistry, Thapar Institute of Engineering and Technology, Patiala-147004, Punjab, India. E-mail: debasish.mandal@thapar.edu

† Electronic supplementary information (ESI) available: Full citation of Gaussian 16, relative energy tables, Mulliken spin and charges, distortion energies, LUMO values for reactants, and optimized Cartesian coordinates for all the stationary points. See DOI: https://doi.org/10.1039/d4dt00063c

Open Access Article. Published on 02 April 2024. Downloaded on 1/23/2026 10:42:30 PM.
This article is licensed under a Creative Commons Attribution-NonCommercial 3.0 Unported Licence.

with a larger oxidation state enhancing the reactivity owing to the electrophilicity and reduction potential.[20,21] Multiple DFT and experimental studies have been performed to explore and enhance the C–H activation processes carried out by such complexes, in which the reactivity is significantly influenced by the thermodynamics of bond formation (O–H) and breakage (C–H). These reactions proceed mostly with simultaneous transfer of electrons and protons (HAT or cPCET mechanism), which has been studied from time to time.[22–24] Here we see how the transfer of an electron and a proton together as a true H atom is referred to as hydrogen atom transfer, but when they travel differently, it is called proton coupled electron transfer. However, it has also been established that in contrast to these mechanisms, proton and electron transfer can take place stepwise[25,26] wherein the transfer involves two steps. These involve PT followed by ET (basic mechanism) or ET followed by PT (oxidative mechanism) as summed in Scheme 1 herein. There might even be asynchronicity involved with the TS consisting of either more electron or proton transfer.

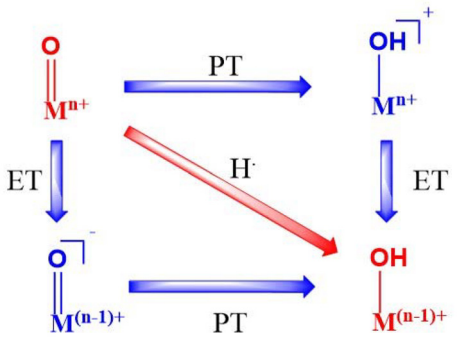

Scheme 1 Various types of mechanisms possible for H transfer.

PT signifies proton transfer whereas ET is electron transfer. Also, the red arrow shows synchronous behaviour and purple the asynchronous. Such mechanisms have a significant role in some cases wherein the otherwise lower oxidation potential is balanced by factors such as the basicity of the metal oxo complexes (*via* PT followed by ET).[27–30]

The developments in this field have given considerable momentum to both the understanding and the application of the Fe(IV)-oxo chemistry in homogeneous catalytic oxidation. Now, let's take into contemplation the well-known fact that the biological Fe═O oxidants in the (IV) oxidation state of the iron atom usually consist of O-based ligands (weak field in nature), *e.g.*, carboxylate, water located *cis* to the oxo donor (Scheme 2a).[31,32]

In our previous work in this field of hetero-substitution, inspired by the study of Ray and co-workers, we highlighted how alterations made in the primary coordination sphere of TMC like complexes in a sequential order (using S) of equatorial ligands resulted in better reactivity trends for the C–H activation process.[33] We successfully established that hetero-substitution led to lower reaction barriers and hence opened the door to the use of alternative atoms in the vastly studied ferryl processes.[34] In a combined experimental and computational study performed by Prez *et al.*, substitution of the N–CH_3 donor in TMC and TMCN macrocycles was studied to depict how this O substitution led to better reactivity patterns. The details of the structures are presented in Scheme 3. Other than the N/O donor atom, there is also a significant difference in the structure between traditional TMC (Scheme 3a) and TMCO (Scheme 3c). The propylene and ethylene linkers are in adjacent positions in TMCO; however, they are in alternate positions in TMC.[35] The axial ligands are also different. In TMCN, CD_3 substituents on the donor N atoms are attached equatorially in place of CH_3 (Scheme 3b).

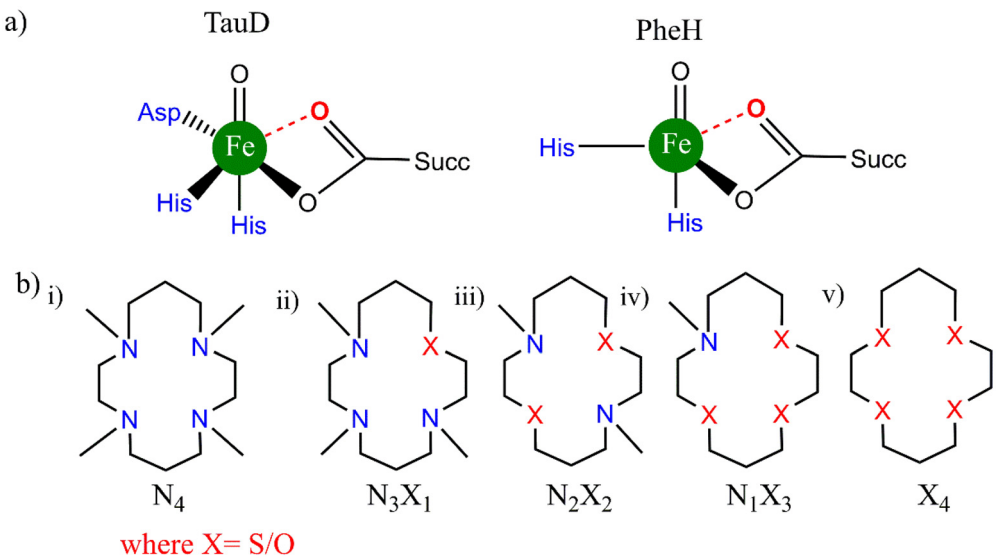

Scheme 2 Structures of (a) biological enzymes taurine:αKG dioxygenase and phenylalanine hydroxylase and (b) bioinspired TMC complexes with equatorial substitution.

 This journal is © The Royal Society of Chemistry 2024

Open Access Article. Published on 02 April 2024. Downloaded on 1/23/2026 10:42:30 PM.
This article is licensed under a Creative Commons Attribution-NonCommercial 3.0 Unported Licence.

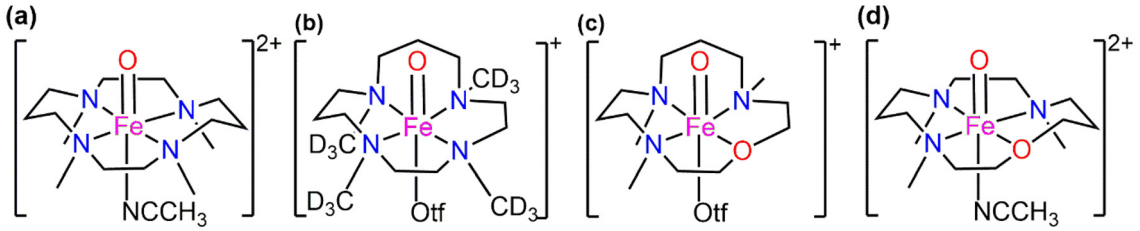

Scheme 3 (a) TMC with CH_3CN as an axial ligand, (b) TMCN with $-OSO_2CF_3$ as an axial ligand, (c) TMCO with $-OSO_2CF_3$ as an axial ligand and (d) TMCO complexes with a similar conformation and axial ligand to TMC.

This encouraged us to investigate the effects on C–H activation reactivity after substituting oxygen for the equatorial donor atom nitrogen. For this purpose, anti-geometric isomers (anti-position of methyl groups w.r.t the Fe═O unit) of the base molecule with the same axial ligand have been used. The most investigated TMC (Scheme 3a) macrocycle has been selected as the base compound which makes the TMCO complex as presented in Scheme 3d. The primary goal here is to determine whether oxygen-substituted iron-oxo TMC complexes may offer us a better C–H activation catalyst and whether these improvements will happen in a sequential manner. Dihydroanthracene (DHA) is used as a C–H bond source and the reaction has been modelled in the presence of the solvent acetonitrile. Reactivity studies have been performed on both lower (S = 1) and higher (S = 2) spin states. The interplay of various other factors has also been taken into consideration which include-spin density on the abstractor atoms, frontier orbitals and deformation energies to obtain the transition states. Mulliken charges and spin have been carefully analysed guiding us to the correct identification of the electronic states. Effects of N, O-substituted macrocycles on quantum mechanical tunneling and the H/D kinetic isotope effect have also been analysed.[36]

Computational details

The DFT method has been used to carry out geometry optimization for all the species wherein the popular B3LYP functional (Becke's three-parameter exchange with Lee, Yang, and Parr's correlation functional) has come to practice.[37–39] Several independent studies support this functional for the C–H activation reaction catalysed by this type of complex, and hence it is a significant benchmark.[40,41] For the study of spin state gaps we have further used the functionals TPSSH and M06-L as presented in Table S7.† For the basis set we have taken (i) LANL2DZ with ECP for Fe and Pople's double zeta 6-31G* for all the other atoms, namely C, H, N, O, F and S marked as B1 for convenience.[42,43] The effect of acetonitrile solvent has been computed during optimization using the self-consistent reaction field *i.e.*, the SCRF and SMD model.[44,45] Further single-point calculations have also been performed for energy refinement using (ii) Def2tzvpp for all atoms marked as B2 and (iii) 6-311++G(2d,2p) for all atoms and ECP containing SDD for iron marked as B3. The same solvent model as for B1 has also been implemented in B2 and B3. Triflate ($CF_3SO_3^-$) counterions are poised at the bottom parts of the axial ligands to make the system neutral. The use of solvents with counterions usually diminishes the secondary interactions by neutralising the charges.[46] Frequency calculations are very detrimental for validating the nature of the optimized structures wherein one imaginary frequency indicates the transition states (TS), and have been performed at the B1 level of theory. The zero-point vibrational energy (ZPVE) and thermal and entropic corrections to the Gibbs free energy at T = 298 K (25 °C) have been evaluated for valid determination of the potential energy surface. Intrinsic reaction coordinate (IRC) calculations have also been carried out to further verify if the TS are connecting to the proper minima as required.[47] This entire DFT study has been performed using Gaussian 16[48] program packages, and for the generation as well as visualisation of natural orbitals, Chemcraft software[49] has been used. For rate, isotope effect and quantum mechanical tunneling studies have been performed using KiSThelP software.[50] The kinetics calculations have been performed using the following equation:[51]

$$k = \kappa\sigma\frac{k_b T}{h}\exp\left(\frac{-\Delta G^{\ddagger}}{RT}\right) \quad (1)$$

where κ and σ stand for the transmission coefficient and reaction symmetry, respectively. The transmission coefficient has been calculated using the 1D (one-dimensional) asymmetric Eckart method[52] which has been used in various H-transfer processes successfuly.[53–55] ZPE corrected energies of the reactant, transition states, and products in addition to the imaginary frequency are used in this method, which in turn build up the mass weighted intrinsic reaction coordinate (IRC).[56] The H/D kinetic isotope effect (KIE) values have been calculated from the respective rate constants from H and D variants as follows:

$$\mathrm{KIE} = \frac{k_H}{k_D} \quad (2)$$

For calculating the reduction of the activation barrier, we have used the following equation where R is the universal gas constant and T is the absolute temperature

$$\Delta\Delta E^{\ddagger}_{tun} = -RT\ln\kappa(T) \quad (3)$$

Open Access Article. Published on 02 April 2024. Downloaded on 1/23/2026 10:42:30 PM.
This article is licensed under a Creative Commons Attribution-NonCommercial 3.0 Unported Licence.

For calculating stability constant $\log\beta$, the following equation has been used.[57]

$$\log\beta = (\log_{10} e)\frac{-\Delta G}{RT} = \frac{-\Delta G}{2.303RT} \quad (4)$$

where R is the universal gas constant and T is the temperature. ΔG has been calculated for the reactions using the following equation:

$$\Delta G = G(\mathrm{ML}) + 4 \times G(\mathrm{H_2O}) - G\{\mathrm{M(H_2O)_4}\} - G(\mathrm{L}) \quad (5)$$

where ML represents the Fe(IV)O(TMC) complexes and L is the respective N_4, N_3O, N_2O_2, NO_3, and O_4 tetradentate macrocyclic ligands.

Distortion energies for the transition state have been calculated using the following equation:

$$\Delta E^{\ddagger}_{\mathrm{dist}} = (E^{\ddagger}_{\mathrm{R}} + E^{\ddagger}_{\mathrm{S}}) - (E_{\mathrm{R}} - E_{\mathrm{S}}) \quad (6)$$

where R and S refer to the reactant and substrate counterparts in the TS structure.

Results

At first, we searched for the potential for production of each of the five Fe(IV)O complexes by figuring out their stability constants, which are represented by $\log\beta$ in eqn (4). Since the constant shows how the ligation of the individual TMC complexes (with varied donor atoms) to the Fe=O unit would affect the free energy of formation, higher values of the constant indicate more favourable complex formation. In all five complexes, stability constant values were determined to be approximately 28.2. Kirby *et al.* in a study of a few U(VI) complexes showed comparable values of $\log\beta$.[57] It is also observed in their case that the calculated values are overestimated with respect to the experimentally observed ones. Here, we are unable to adequately support the absolute values of $\log\beta$ because there is a dearth of literature on stability constants for Fe(IV)O. Aside from the absolute value, however, we can declare with confidence that the O-substituted TMC macrocycle can ligate with Fe(IV)O in a manner similar to that of the most popular N_4 TMC frameworks. The optimized geometries of the quintet oxidants with important parameters are presented in Fig. 1.

While the average Fe–N/Fe–O distance (equatorially linked) decreased progressively, the Fe=O and Fe–N_{ax} bond lengths (axially connected) are almost the same in all complexes.

Spin state reactivity

In general, the four unpaired electrons in Fe(IV) can be occupied in a variety of ways, resulting in two distinct spin states, S = 1 and S = 2. Thus, the hydrogen atom transfer mechanism can occur in either or both states[58] and the electron transfer pathways are presented in Fig. 2.

The panel a of Fig. 2 shows the low spin *i.e.* triplet state pathway where a β electron from the σ_{C-H} bond moves to one

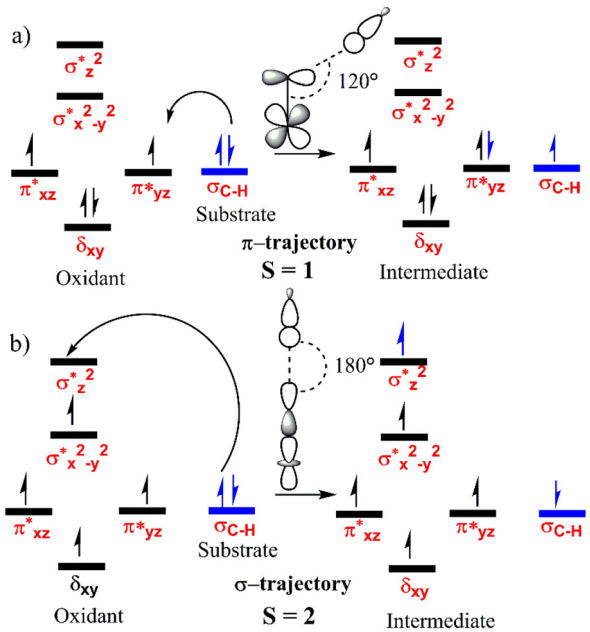

Fig. 2 The general electron transfer mechanism for the HAT catalysed by the Fe(IV)O complexes for spin states (a) S = 1 and (b) S = 2.

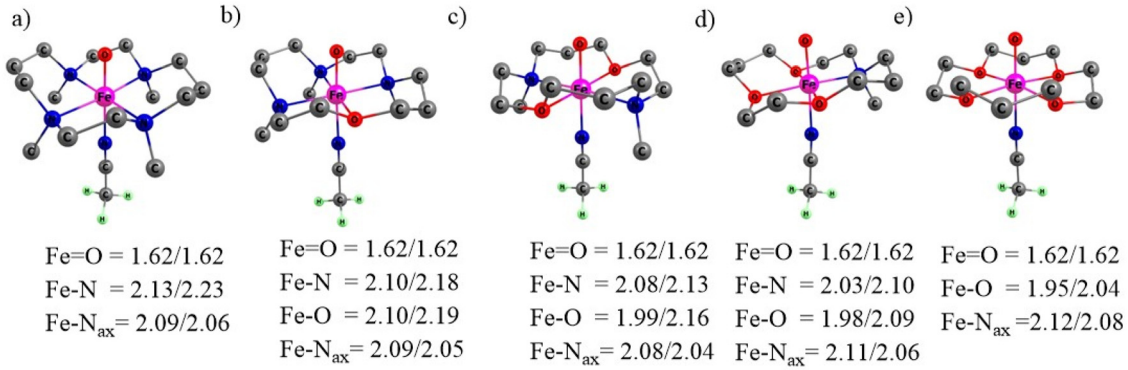

Fig. 1 The optimized oxidants with geometrical parameters with S = 1/S = 2, wherein distances are in Å (a) N_4, (b) N_3O_1, (c) N_2O_2, (d) N_1O_3 and (e) O_4. Hydrogen atoms are omitted for clarity.

Open Access Article. Published on 02 April 2024. Downloaded on 1/23/2026 10:42:30 PM.
This article is licensed under a Creative Commons Attribution-NonCommercial 3.0 Unported Licence.

of the π* orbitals of Fe. This is referred to as the π pathway/trajectory since the transfer takes place to the π* orbital.[59] As depicted, the orientation of the substrate occurs at an Fe–O–H angle of ~120°. The panel b shows the high spin path *i.e.* the quintet pathway where one α electron from the σ_{C-H} bond of the DHA shifts to the $\sigma^*_{z^2}$ anti-bonding orbital of Fe. Here, as DHA approaches the oxidant through the upper side with an Fe–O–H angle of ~180°, this pathway is named the σ pathway/trajectory.

Reactivity pattern

Reactants in the quintet state typically have higher energy than reactants in the triplet state for Fe(IV)=O complexes; however, this is reversed in the transition state and product, leading to the Two-State-Reactivity (TSR) phenomenon. Fig. 3 depicts all the relevant potential energy surfaces for the rate determining step of the C–H activation process catalysed by all five complexes.

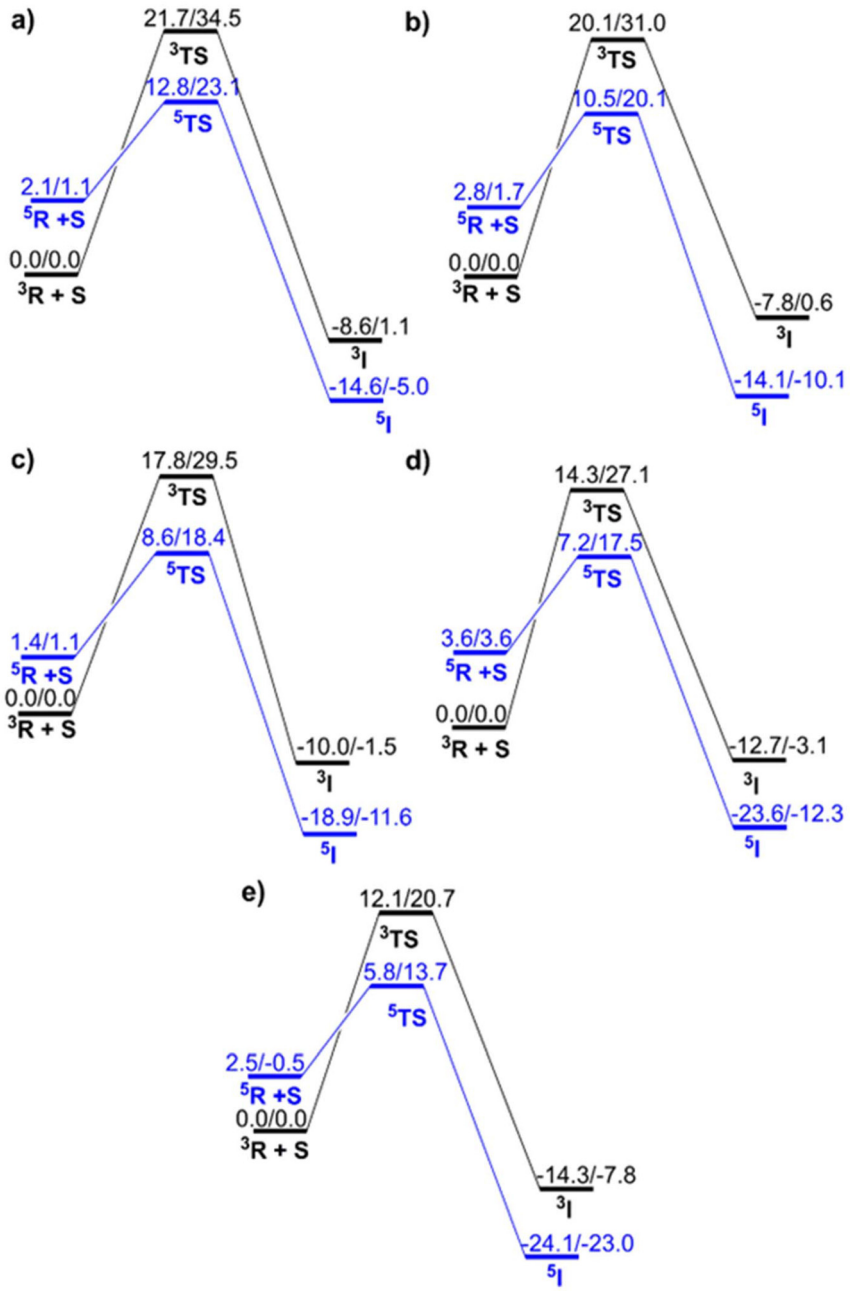

Fig. 3 The potential energy surface for the C–H activation catalysed by the Fe(IV)O complex with (a) N_4, (b) N_3O_1, (c) N_2O_2, (d) N_1O_3 and (e) O_4 macrocyclic ligands. The black and blue lines represent the S = 1 and S = 2 state pathways, respectively. The energy values are given as ΔE(B2+ZPE)/$\Delta G_{298\ K}$(B2). The PESs are plotted with respect to the energy of ^{3}R + DHA.

Open Access Article. Published on 02 April 2024. Downloaded on 1/23/2026 10:42:30 PM.
This article is licensed under a Creative Commons Attribution-NonCommercial 3.0 Unported Licence.

$S = 1$ is observed as the ground state in all oxidants, and the spin state energy gaps (ΔE_{Q-T}) are 2.1, 2.8, 1.4, 3.6, and 2.5 for N_4, N_3O_1, N_2O_2, N_1O_3, and O_4, respectively. As a manifestation of exchange enhanced reactivity,[60] TSR is observed here.[61–64]

In this instance an interesting reactivity pattern is observed. The C–H activation barrier for catalysis by five different oxidants is observed to decrease in a sequential manner with the increasing amount of oxygen substitution in the TMC macrocycle. Regardless of the choice of the basis set or thermodynamic parameters used, such as free energy or ZPE corrected energy, the reactivity pattern remains consistent. In the B2 level of theory the barrier of activation values kept decreasing as 12.82 (23.14) (N_4) > 10.50 (20.06) (N_3O_1) > 8.59 (18.38) (N_2O_2) > 7.19 (17.52) (N_1O_3) > 5.79 (13.73) (O_4) wherein the values in the brackets indicate free energies. The free energy trend at B3 appeared to be 20.90 for N_4, 15.80 for N_3O_1, 14.76 for N_2O_2, 13.16 for N_1O_3 and 12.24 for O_4. Even on comparing the values for triplet states of all the complexes, respectively, we observed the same trend of reactivity *i.e.*, $N_4 < N_3O_1 < N_2O_2 < N_1O_3 < O_4$. By comparing the energies and free energies of the intermediates (Fe(III)OH···$^{\bullet}$R), specifically in the quintet state, it is found that substituting nitrogen with oxygen in the macrocycle results in increased exothermicity of the reaction. This may be attributed to the reduction in energy of the d_{z^2} orbital, which decreases sequentially with each O-replacement. However, this replacement had no substantial effect on the energy of the $d_{x^2-y^2}$ orbital; therefore, the ΔE_{Q-T} in the reactant remained essentially unchanged. All these data have been presented in Table S1.† This led us to divulge into the contributing cause of this kind of fascinating pattern. As the spin state gaps are identical in all the complexes and $S = 1$ is the ground state for reactants, we observed a crossover to the $S = 2$ surface during TSR, and this led us to take into consideration factors other than the triplet–quintet gap which are discussed in detail below.

Spin density

The spin density on the abstractor, *i.e.*, on the oxygen of Fe═O, plays a key role in the reaction dynamics.[65] On evaluating these values on the O atom of the ferryl group in the TS we observed a sequential increase from 0.28 (N_4) to 0.30 (N_3O_1) to 0.33 (N_2O_2) to 0.35 (N_1O_3) to 0.40 (O_4). In the plot in Fig. 4, we notice a sufficiently linear connection ($R^2 = 0.93$) between the spin density on the abstractor and the energy of activation.

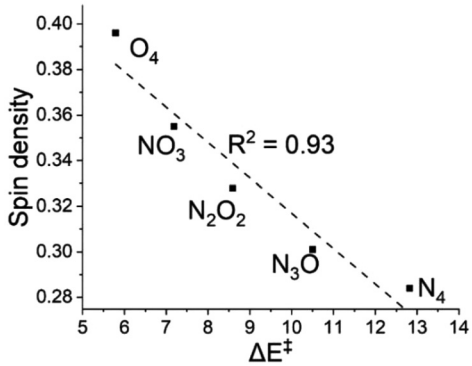

Fig. 4 A plot of activation energy ($\Delta E^{\ddagger}$) *versus* spin density at the 'O' of the Fe═O unit in the $S = 2$ transition state.

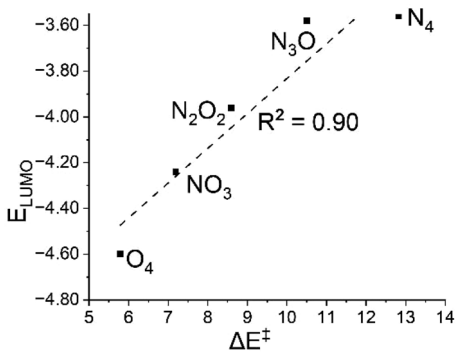

Fig. 5 A plot of activation energy ($\Delta E^{\ddagger}$) *versus* the energy of the LUMO *i.e.*, the electron acceptor orbital (E_{LUMO}) of the oxidants at the $S = 2$ state.

LUMO energies

The acceptor orbital's energy has a significant impact on the reactivity of electron transfer processes. In the $S = 2$ state of these oxidants, the electron acceptor orbital ($\sigma^*_{z^2}$) is the lowest unoccupied molecular orbital (LUMO), and its lower energy values make the electron transfer from the substrate easier. Therefore, the trend −3.56 (N_4) to −3.58 (N_3O_1) to −3.96 (N_2O_2) to −4.24 (N_1O_3) to −4.60 (O_4) showed that the process of accepting electrons from DHA became more convenient as we continued to replace N atoms with O. This is one of the prominent reasons for the increased reactivity with this heterosubstitution.[33,34] As depicted in Fig. 5, the linear relationship between activation energy and LUMO energy provides insight into reactivity.

The lowering tendency in LUMO energy could have resulted from oxygen having a weaker field effect than nitrogen, which in turn stabilises the anti-bonding acceptor orbital. This can be explained on the basis of charge transfer. We performed NBO and Mulliken population analyses to see how on moving from N_4 to O_4 the charge transferred from the ligands attached to the metal centre. As more and more charges were transferred, the trend at the Fe atoms was 0.55 (N_4) to 0.61 (N_3O_1) to 0.64 (N_2O_2) to 0.73 (N_1O_3) to 0.81 (O_4), and it is safe to say that the ligand field kept on weakening sequentially resulting in a more electrophilic metal centre and hence more reactivity.

Distortion energies

To further validate our results, we then used eqn (6) from the Computational details section to determine the distortion energies ($\Delta E^{\ddagger}_{dist}$) of the oxidants and substrate in order to reach the transition states. A plot of $\Delta E^{\ddagger}_{dist}$ and the energy of activation is presented in Fig. 6.

Fig. 6 demonstrates a consistent decrease in $\Delta E^{\ddagger}_{dist}$, with the greatest value of 13.1 in N_4; other values are 12.4 for N_3O_1,

Open Access Article. Published on 02 April 2024. Downloaded on 1/23/2026 10:42:30 PM.
This article is licensed under a Creative Commons Attribution-NonCommercial 3.0 Unported Licence.

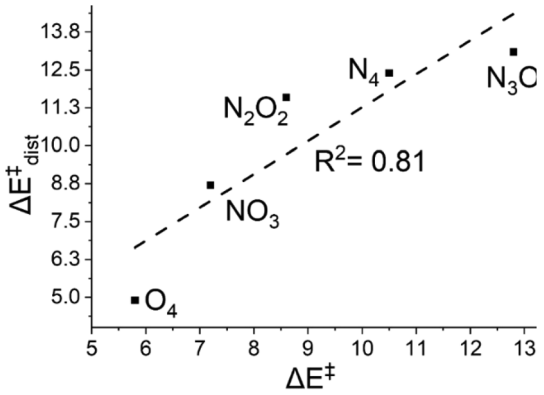

Fig. 6 A plot of activation energy ($\Delta E^{\ddagger}$, in kcal mol^{-1}) *versus* the distortion energies ($\Delta E^{\ddagger}_{dist}$, in kcal mol^{-1}) of the oxidants at the S = 2 state.

11.6 and 8.7 for N_2O_2 and N_1O_3, respectively, and 4.9 for O_4. Lower distortion energies in the oxygen-substituted complexes show how the distortion undergone is minimum in these cases and hence the formation of the transition state is more favourable.

Our findings also show good consistency with earlier research in related complexes, which published theoretical calculations and experimentally validated investigations for TMC and TMCO complexes (Scheme 3a and c). The B3LYP/TDZP estimated free energy of activation for the cyclohexene substrate indicates that the TMCO complex was more favourable than the TMC-N4 by 6.3 kcal mol^{-1}.[35] Here for the DHA substrate we found a similar value, 5.1 kcal mol^{-1}, in the B3 level of theory.

Quantum chemical tunneling

We were also curious to look for the impact of 'O' substitution on quantum mechanical tunneling. The data related to the tunneling calculation of the H-abstraction reaction catalysed by all five complexes are presented in Table 1.

Standard TMC complexes (N4) have a tunneling corrected H/D kinetic isotope effect of 12.5, which is in good accord with an earlier empirically reported value of 10.[66] It's interesting to note that when 'O' is substituted on TMC, the transmission coefficient and KIE fall progressively. The values of the tunneling adjusted KIE are 12.5 (N_4), 7.9 (N_3O_1), 5.3 (N_2O_2), 3.3 (N_1O_3), and 2.0 (O_4) as shown in column 6 of Table 1.

It is revealed that the imaginary frequency of the transition states, which regulates the potential energy surface's curvature, is the cause of this pattern. Higher tunneling is insinuated by a narrower curvature, which is implied by a higher imaginary frequency value.[40] Fig. 7 presents the transition state structures with significant geometrical features and imaginary frequencies.

The imaginary frequency value for N_4 is 1231.2i, and it decreases steadily to 986.7i for N_3O_1, 811.5i for N_2O_2 and 416.6i for O_4 and 165.3i for N_1O_3. In the context of breaking C–H and forming O–H bond parameters in the transition state it is clear that the transition state for N_4 is most symmetric. The C–H bond keeps becoming shorter from N_4 to O_4, and oppositely, the O–H bond distances keep increasing, making the TS product-like in prior cases but reactant-like in the latter.

So, the decreasing frequencies with the substitution taking place hint at the role of quantum tunneling since it's a well-known fact that the mechanism of QM tunneling (quantum mechanical tunneling) relies on the path function, and poten-

Table 1 The value of rate constants for the H-abstraction reactions (k_H and k_D in cm^3 per molecule per second), transmission coefficients (κ_H and κ_D), kinetic isotope effect (KIE_{ECK}), barrier lowering quantity ($\Delta\Delta E^{\ddagger}_{tun}$), and the effective barrier ($\Delta E - \Delta\Delta E^{\ddagger}_{tun}$)

Complex	k_H	k_D	κ_H	κ_D	KIE_{ECK}	$\Delta\Delta E^{\ddagger}_{tun}$	$\Delta E - \Delta\Delta E^{\ddagger}_{tun}$
N_4	8.12×10^{-25}	6.48×10^{-26}	6.61	2.96	12.5 (10)[a]	1.12	11.7
N_3O	3.44×10^{-23}	4.38×10^{-24}	3.04	2.03	7.9	0.66	9.8
N_2O_2	2.20×10^{-22}	4.15×10^{-23}	2.05	1.64	5.3	0.42	8.2
NO_3	2.17×10^{-20}	6.55×10^{-21}	1.19	1.64	3.3	0.10	7.1
O_4	3.65×10^{-20}	1.82×10^{-20}	1.03	1.02	2.0	0.01	5.8

[a] The value in parentheses is the experimental value.[66]

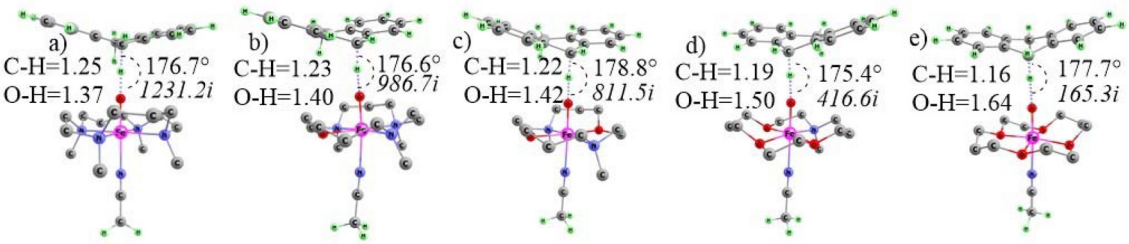

Fig. 7 Quintet TS with their imaginary frequencies for (a) N_4, (b) N_3O_1, (c) N_2O_2, (d) N_1O_3 and (e) O_4 macrocyclic ligands with C–H (breaking) and O–H (forming) bond lengths.

Open Access Article. Published on 02 April 2024. Downloaded on 1/23/2026 10:42:30 PM.
This article is licensed under a Creative Commons Attribution-NonCommercial 3.0 Unported Licence.

tial energy surfaces (PES) depend on the imaginary frequencies. Higher imaginary frequencies indicate a sharper PES, *i.e.*, an atom has to tunnel through a shorter distance making the phenomenon more favourable. The tunneling coefficients for H and D isotope counterparts with Eckart corrected values of KIE are reported herein. We have also calculated the tunneling corrected barrier. When switching from N_4 to O_4, the calculated natural charges on Fe in the $S = 2$ oxidant are nearly equal with oxygen replacement, *i.e.*, 0.95, 0.94, 0.93, 0.95, and 0.97. It follows that anti-electrophilicity has no influence on tunneling in this situation.[40]

Although the reduction of the activation barrier by tunneling (column 7 in Table 1) is higher in N_4 (due to the higher transmission coefficient), the overall effective barrier (column 8 in Table 1) is not able to alter the earlier reactivity pattern obtained from classical thermodynamics.

Conclusions

This computational study has been devoted to investigating the reactivity of the oxygen substituted iron(IV)-oxo N_4 macrocycle in order to design a better catalyst for C–H activation. A well-known TMC compound, $[Fe(IV){=}O(TMC\text{-}N_4)(CH_3CN)]^{2+}$, has been taken into consideration for base compounds. Additionally, the method of sequentially replacing the equatorial N atoms with O atoms results in the formation of four additional compounds with frameworks consisting of N_4, N_3O_1, N_2O_2, N_1O_3, and O_4. The computed values of the stability constants support the formation of these complexes, which proved to be as beneficial as the main compound N_4. The hydrogen atom transfer from dihydroanthracene, *i.e.*, the rate determining step of the C–H activation, has been investigated in both triplet and quintet spin states. Due to the presence of exchange enhanced reactivity and the two-state-reactivity phenomenon, $S = 2$ was found to be more reactive in all five cases. An interesting reactivity trend is observed, namely, the C–H activation reactivity gradually increases with the enrichment of 'O' in TMC macrocycles, *i.e.*, $N_4 < N_3O_1 < N_2O_2 < N_1O_3$, and O_4, irrespective of the computed levels of theories. The increased reactivity in the substituted compounds may be to some extent explained by the TS being reactant-like for the oxygen substituted TMC, as shown by the length of the breaking and forming bonds. This is further reflected in the distortion energy pattern, where the substituted TMC complexes require progressively less energy. Given that the spin state gap remains consistent across all complexes, it is not the primary determining factor in this scenario. Additionally, the energy of the electron acceptor orbital, or LUMO energy, which progressively drops with the number of oxygen-enriched macrocycles, was likewise connected with the reactivity pattern. The weak ligand field on moving from N4 to O4 is evident from the charge transfer values. An interesting pattern was also observed in the case of quantum mechanical tunneling (QMT) and H/D KIE, which continually decreases with transformation from N_4 to O_4. This might be explained by the broad H-transfer curvature as predicted by the low imaginary frequencies in the transition states. The barrier reduction amount by QMT was not significant enough to alter the classical reactivity trend. Our results are also in line with the previous studies conducted on TMC like complexes. Finally, these studies if carried out experimentally will make a path for alternative complexes other than typical N complexes and hence lead to new choices in this bioinorganic field.

Conflicts of interest

There are no conflicts to declare.

Acknowledgements

D. Mandal is very grateful to the Department of Science and Technology, Government of India, for providing the INSPIRE Faculty Fellowship (DST/INSPIRE/04/2016/001948) and for a Thapar Institute of Engineering and Technology SEED grant (TU/DORSP/57/7278).

References

1 V. A. Larson, B. Battistella, K. Ray, N. Lehnert and W. Nam, *Nat. Rev. Chem.*, 2020, **4**, 404–419.
2 H. Hirao, F. Li, L. Que and K. Morokuma, *Inorg. Chem.*, 2011, **50**, 6637–6648.
3 H. Schwarz and S. Shaik, *Metal-Oxo and Metal-Peroxo Species in Catalytic Oxidations*, 2000.
4 T. Z. H. Gani and H. J. Kulik, *ACS Catal.*, 2018, **8**, 975–986.
5 J. England, J. O. Bigelow, K. M. Van Heuvelen, E. R. Farquhar, M. Martinho, K. K. Meier, J. R. Frisch, E. Münck and L. Que, *Chem. Sci.*, 2014, **5**, 1204–1215.
6 W. Nam, Y. M. Lee and S. Fukuzumi, *Acc. Chem. Res.*, 2014, **47**, 1146–1154.
7 K. Rydel-Ciszek, *React. Kinet., Mech. Catal.*, 2021, **133**, 579–600.
8 A. N. Biswas, M. Puri, K. K. Meier, W. N. Oloo, G. T. Rohde, E. L. Bominaar, E. Münck and L. Que, *J. Am. Chem. Soc.*, 2015, **137**, 2428–2431.
9 Y. Wang and K. Han, *J. Biol. Inorg. Chem.*, 2010, **15**, 351–359.
10 S. P. de Visser, M. G. Quesne, B. Martin, P. Comba and U. Ryde, *Chem. Commun.*, 2014, **50**, 262–282.
11 E. Masferrer-Rius, M. Borrell, M. Lutz, M. Costas and R. J. M. Klein Gebbink, *Adv. Synth. Catal.*, 2021, **363**, 3783–3795.
12 C. A. Joseph and M. J. Maroney, *Chem. Commun.*, 2007, 3338–3349.
13 M. Sallmann, S. Kumar, P. Chernev, J. Nehrkorn, A. Schnegg, D. Kumar, H. Dau, C. Limberg and S. P. De Visser, *Chem. – Eur. J.*, 2015, **21**, 7470–7479.
14 A. J. Johansson, M. R. A. Blomberg and P. E. M. Siegbahn, *J. Phys. Chem. C*, 2007, **111**, 12397–12406.

 This journal is © The Royal Society of Chemistry 2024

Open Access Article. Published on 02 April 2024. Downloaded on 1/23/2026 10:42:30 PM.
This article is licensed under a Creative Commons Attribution-NonCommercial 3.0 Unported Licence.

15 W. Nam, *Acc. Chem. Res.*, 2007, **40**, 522–531.
16 S. Impeng, S. Siwaipram, S. Bureekaew and M. Probst, *Phys. Chem. Chem. Phys.*, 2017, **19**, 3782–3791.
17 K. Warm, A. Paskin, U. Kuhlmann, E. Bill, M. Swart, M. Haumann, H. Dau, P. Hildebrandt and K. Ray, *Angew. Chem., Int. Ed.*, 2021, **60**, 6752–6756.
18 H. Park and D. Lee, *Chem. – Eur. J.*, 2020, **26**, 5916–5926.
19 C. V. Sastri, J. Lee, K. Oh, J. L. Yoon, J. Lee, T. A. Jackson, K. Ray, H. Hirao, W. Shin, J. A. Halfen, J. Kim, L. Que, S. Shaik and W. Nam, *Proc. Natl. Acad. Sci. U. S. A.*, 2007, **104**, 19181–19186.
20 R. Kumar, B. Pandey, A. Sen, M. Ansari, S. Sharma and G. Rajaraman, *Coord. Chem. Rev.*, 2020, 419.
21 A. Ansari, A. Kaushik and G. Rajaraman, *J. Am. Chem. Soc.*, 2013, **135**, 4235–4249.
22 M. Mandal, C. E. Elwell, C. J. Bouchey, T. J. Zerk, W. B. Tolman and C. J. Cramer, *J. Am. Chem. Soc.*, 2019, **141**, 17236–17244.
23 J. E. M. N. Klein and G. Knizia, *Angew. Chem., Int. Ed.*, 2018, **57**, 11913–11917.
24 J. M. Mayer, *Acc. Chem. Res.*, 2011, **44**, 36–46.
25 D. Usharani, D. C. Lacy, A. S. Borovik and S. Shaik, *J. Am. Chem. Soc.*, 2013, **135**, 17090–17104.
26 M. K. Goetz and J. S. Anderson, *J. Am. Chem. Soc.*, 2019, **141**, 4051–4062.
27 T. H. Yosca, J. Rittle, C. M. Krest, E. L. Onderko, A. Silakov, J. C. Calixto, R. K. Behan and M. T. Green, *Science*, 2013, **342**, 825–829.
28 M. T. Green, J. H. Dawson and H. B. Gray, *Science*, 2004, **304**, 1653–1656.
29 P. J. Donoghue, J. Tehranchi, C. J. Cramer, R. Sarangi, E. I. Solomon and W. B. Tolman, *J. Am. Chem. Soc.*, 2011, **133**, 17602–17605.
30 D. Dhar, G. M. Yee, T. F. Markle, J. M. Mayer and W. B. Tolman, *Chem. Sci.*, 2017, **8**, 1075–1085.
31 N. I. Burzlaff, P. J. Rutledge, I. J. Clifton, C. M. H. Hensgens, M. Pickford, R. M. Adlington, P. L. Roach and J. E. Baldwin, *Nature*, 1999, **401**, 721–724.
32 P. L. Roach, I. J. Clifton, C. M. H. Hensgens, N. Shibata, C. J. Schofield, J. Hajdu and J. E. Baldwin, *Nature*, 1997, **387**, 827–830.
33 J. Deutscher, P. Gerschel, K. Warm, U. Kuhlmann, S. Mebs, M. Haumann, H. Dau, P. Hildebrandt, U. P. Apfel and K. Ray, *Chem. Commun.*, 2021, **57**, 2947–2950.
34 L. Kaur and D. Mandal, *Inorg. Chem.*, 2022, **61**, 14582–14590.
35 I. Monte Pérez, X. Engelmann, Y. M. Lee, M. Yoo, E. Kumaran, E. R. Farquhar, E. Bill, J. England, W. Nam, M. Swart and K. Ray, *Angew. Chem., Int. Ed.*, 2017, **56**, 14384–14388.
36 A. Katoch and D. Mandal, *Dalton Trans.*, 2022, **51**, 11641–11649.
37 A. D. Becke, *J. Chem. Phys.*, 1993, **98**, 1372–1377.
38 A. D. Becke, *J. Chem. Phys.*, 1996, **104**, 1040–1046.
39 A. Altun, J. Breidung, F. Neese and W. Thiel, *J. Chem. Theory Comput.*, 2014, **10**, 3807–3820.
40 J. E. M. N. Klein, D. Mandal, W. M. Ching, D. Mallick, L. Que and S. Shaik, *J. Am. Chem. Soc.*, 2017, **139**, 18705–18713.
41 D. Mandal, D. Mallick and S. Shaik, *Acc. Chem. Res.*, 2018, **51**, 107–117.
42 Y. Yang, M. N. Weaver and K. M. Merz, *J. Phys. Chem. A*, 2009, **113**, 9843–9851.
43 P. J. Hay and W. R. Wadt, *J. Chem. Phys.*, 1985, **82**, 299–310.
44 A. V. Marenich, C. J. Cramer and D. G. Truhlar, *J. Phys. Chem. B*, 2009, **113**, 6378–6396.
45 A. V. Marenich, R. M. Olson, C. P. Kelly, C. J. Cramer and D. G. Truhlar, *J. Chem. Theory Comput.*, 2007, **3**, 2011–2033.
46 D. Janardanan, D. Usharani, H. Chen and S. Shaik, *J. Phys. Chem. Lett.*, 2011, **2**, 2610–2617.
47 S. Maeda, Y. Harabuchi, Y. Ono, T. Taketsugu and K. Morokuma, *Int. J. Quantum Chem.*, 2015, **115**, 258–269.
48 E. B. Bauer, *Isr. J. Chem.*, 2017, **57**, 1131–1150.
49 J. P. Cerón-Carrasco and D. Jacquemin, *Phys. Chem. Chem. Phys.*, 2013, **15**, 4548–4553.
50 S. Canneaux, F. Bohr and E. Hénon, *J. Comput. Chem.*, 2014, **35**, 82–93.
51 H. Eyring, *J. Chem. Phys.*, 1935, **3**, 63–71.
52 C. Eckart, *Phys. Rev.*, 1930, **35**, 1303–1309.
53 D. K. Maity, R. L. Bell and T. N. Truong, *J. Am. Chem. Soc.*, 2000, **122**, 897–906.
54 F. Zhang and T. S. Dibble, *Phys. Chem. Chem. Phys.*, 2011, **13**, 17969–17977.
55 A. G. Vandeputte, M. K. Sabbe, M. F. Reyniers, V. Van Speybroeck, M. Waroquier and G. B. Marin, *J. Phys. Chem. A*, 2007, **111**, 11771–11786.
56 C. Gonzalez and H. B. Schlegel, *J. Chem. Phys.*, 1991, **95**, 5853–5860.
57 M. E. Kirby, A. Simperler, S. Krevor, D. J. Weiss and J. L. Sonnenberg, *J. Phys. Chem. A*, 2018, **122**, 8007–8019.
58 A. Sirjoosingh and S. Hammes-Schiffer, *J. Phys. Chem. A*, 2011, **115**, 2367–2377.
59 S. A. Wilson, J. Chen, S. Hong, Y. M. Lee, M. Clémancey, R. Garcia-Serres, T. Nomura, T. Ogura, J. M. Latour, B. Hedman, K. O. Hodgson, W. Nam and E. I. Solomon, *J. Am. Chem. Soc.*, 2012, **134**, 11791–11806.
60 D. Janardanan, Y. Wang, P. Schyman, L. Que and S. Shaik, *Angew. Chem.*, 2010, **122**, 3414–3417.
61 D. Mandal, R. Ramanan, D. Usharani, D. Janardanan, B. Wang and S. Shaik, *J. Am. Chem. Soc.*, 2015, **137**, 722–733.
62 C. Geng, S. Ye and F. Neese, *Angew. Chem., Int. Ed.*, 2010, **49**, 5717–5720.
63 S. P. De Visser, *J. Am. Chem. Soc.*, 2006, **128**, 15809–15818.
64 S. Ye, C. Y. Geng, S. Shaik and F. Neese, *Phys. Chem. Chem. Phys.*, 2013, **15**, 8017–8030.
65 J. England, J. Prakash, M. A. Cranswick, D. Mandal, Y. Guo, E. Münck, S. Shaik and L. Que, *Inorg. Chem.*, 2015, **54**, 7828–7839.
66 C. V. Sastri, J. Lee, K. Oh, J. L. Yoon, J. Lee, T. A. Jackson, K. Ray, H. Hirao, W. Shin, J. A. Halfen, J. Kim, L. Que, S. Shaik and W. Nam, *Proc. Natl. Acad. Sci. U. S. A.*, 2007, **104**, 19181–19186.